ACS Sustainable Chemistry & Engineering

pubs.acs.org/journal/ascecg

Research Article

A Dual-Function Poly(vinyl alcohol) Hydrogel for Solar Water Production and Thermoelectric Energy Generation

Yu-Hao Wang, Ching-Chieh Hsu, Shao-Huan Hong, Jian-Fa Ding, U-Ser Jeng, Dun-Yen Kang, Shyh-Chyang Luo, Shih-Huang Tung, and Cheng-Liang Liu*

Cite This: *ACS Sustainable Chem. Eng.* 2025, 13, 4231−4241

Read Online

ACCESS | Metrics & More | Article Recommendations | Supporting Information

ABSTRACT: This work addresses the dual challenges of seawater purification and converting low-grade waste heat into electricity, both of which are crucial for sustainable resource management. It presents a combined approach that solves both problems using a self-fabricated device. The device generates a temperature gradient through efficient photothermal conversion by placing thermoelectric hydrogels on top of a photothermal hydrogel. Poly(vinyl alcohol) (PVA) is used as the matrix for the photothermal hydrogel and was selected for its biocompatibility and ease of processing. In order to enhance both the solar-driven water evaporation and photothermal conversion efficiency, ball-milled dititanium trioxide (Ti_2O_3) nanoparticles and carbon nanotubes (CNTs) are incorporated within the PVA matrix. This approach enables a water evaporation rate as high as 3.22 kg m^{-2} h^{-1}. Additionally, PVA also serves as the matrix for thermoelectric gels, which are soaked with a $K_3[Fe(CN)_6]/K_4[Fe(CN)_6]$ redox pair solution to exploit the thermogalvanic acid (TGC) effect. This arrangement enables voltage generation through redox reactions at the hot and cold ends. The obtained excellent thermoelectric properties can be characterized by the ionic Seebeck coefficient (S_i) of 1.48 mV K^{-1} and a power density of 9.6 mW m^{-2} after nine thermoelectric hydrogels were connected in series. As a result, this dual-functional device simultaneously and effectively purifies seawater and generates electricity. Outdoor testing shows a daily water production of 9.2 kg m^{-2} and a stable voltage generation of 130 mV from the thermoelectric hydrogels. This approach advances water purification and energy generation technologies and opens new avenues for innovative applications in renewable energy.

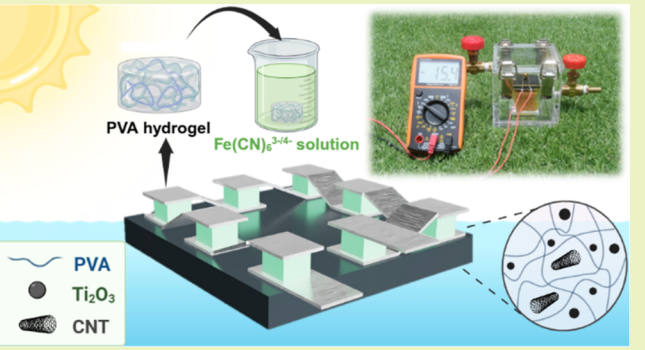

KEYWORDS: *hydrogel, thermoelectric, photothermal, water purification, waste heat harvesting*

INTRODUCTION

The rapid growth of the global population, combined with the intensification of extreme weather events, has worsened water and energy shortages, particularly in remote regions with limited infrastructure.[1−3] Addressing water and energy scarcity is crucial for the continued progress of mankind in the 21st century.[4] Solar energy has become a rapidly advancing and indispensable solution for renewable energy sources. Modern technologies have enabled the efficient conversion of solar energy into usable forms, primarily electricity and thermal energy. This offers a sustainable and environmentally friendly alternative to conventional fossil fuels.[5,6] There are several methods to convert solar radiation to usable energy. Solar thermal conversion uses sunlight to directly convert it into heat. This process is both simple and efficient, with applications in diverse fields such as power generation and seawater desalination.[7,8] Utilizing solar energy for seawater desalination is particularly promising, as it integrates the evaporation of seawater with the removal of impurities and pollutants, yielding clean water.[9−11] Combining solar thermal conversion with other technologies, such as thermoelectric modules or photovoltaic cells, offers an integrated solution that can simultaneously address water and energy shortages.[12,13] Thermoelectric power, driven by sunlight, is a promising approach to convert solar energy into electricity. This approach essentially enhances the thermoelectric device performance through heat conversion. In this case, a temperature gradient (ΔT) is applied to a thermoelectric material, where one side is heated (T_H) and the other is maintained at a lower temperature (T_C). This results in a voltage gradient (ΔV) due to the Seebeck effect, which is characterized by the Seebeck coefficient (S).[14−18]

Received: December 29, 2024
Revised: February 25, 2025
Accepted: February 26, 2025
Published: March 5, 2025

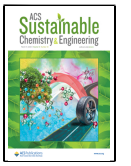

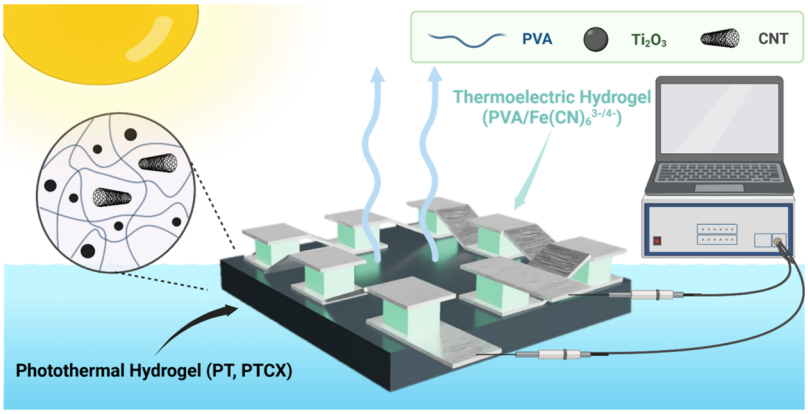

Figure 1. Schematic illustration of dual-function photothermal and thermoelectric hydrogels for simultaneous water evaporation and waste heat harvesting.

Furthermore, porous hydrogels have gained attention for their use in solar evaporators due to their hydrophilicity and ability to reduce the evaporation enthalpy of water.[19−22] For example, Yu et al. developed poly(vinyl alcohol) (PVA) hydrogels embedded with biomass and konjac glucomannan, together with simple-to-fabricate, iron-based metal−organic framework-derived photothermal nanoparticles to regulate the water state, thereby enhancing solar evaporation efficiency.[23,24] Yang et al. introduced a hybrid system based on a piece of carbon-nanotube-modified filter paper and a commercial Nafion membrane that not only extracts freshwater from seawater but also generates electricity. This was done by utilizing the salinity gradient created by solar evaporation. Under 1 kW m^{-2} solar irradiation, this system achieved a water production rate of 1.1 kg m^{-2} h^{-1} and generated approximately 1 W m^{-2} of electricity.[24] Similarly, Ren et al. used a PVA hydrogel and carbon black (CB) immersed in different salt solutions. The group reported an evaporation rate of 3.52 kg m^{-2} h^{-1}. When assembled with *commercial* thermoelectric modules, this system generated an open-circuit voltage of 160 mV and a power density of 0.65 W m^{-2} under 1 kW m^{-2} solar irradiation.[25] Mu et al. proposed a thermoelectricity-freshwater cogenerator based on a thermoelectric generator (TEG) and a starch−polyacrylamide (S-PAM) hydrogel. Their approach reached an evaporation rate of 1.79 kg m^{-2} h^{-1} and a maximum power density of 11.39 W m^{-2} under similar irradiation conditions. This system collected 0.92 kg m^{-2} of water in natural sunlight over 8 h.[26] Despite these advancements, the long-term performance of hydrogels in seawater-based thermoelectric devices remains unsatisfying due to salt accumulation and the potential corrosion of thermoelectric modules from prolonged seawater exposure. Therefore, this study focuses on ways of preventing direct immersion of the thermoelectric device in seawater, which should improve both durability and performance.

In this study, we develop PVA-based dual-function hydrogels that combine good photothermal properties with excellent thermoelectric properties. These hydrogels also feature improved stability concerning dehydration, which can be attributed to the steam generated during the water evaporation process. Furthermore, the hydrogels were embedded with ball-milled Ti_2O_3 nanoparticles (NPs) and CNTs to improve the photothermal conversion efficiency. Under solar irradiation of 1 kW m^{-2}, the photothermal hydrogel demonstrated a high evaporation rate of 3.22 kg m^{-2} h^{-1}. Moreover, when nine thermoelectric hydrogels were connected in series, the device reached a power density of 9.6 mW m^{-2}. Field testing revealed daily water production of 9.2 kg m^{-2}, and stable voltage output could be sustained over 10 h in outdoor conditions. This dual-function device offers a feasible solution for addressing water and energy scarcity, particularly in remote or resource-limited areas, by combining solar-driven water evaporation with electricity generation.

RESULTS AND DISCUSSION

In order to enable simultaneous water evaporation and power generation, we investigated a device that combines photothermal and thermoelectric hydrogels (Figure 1). The photothermal hydrogel (PT, PTCX) is placed in seawater, and upon illumination, the seawater evaporates through the hydrogel network structure to generate purified water. For photothermal materials, Ti_2O_3 nanoparticles were specifically chosen due to their strong near-infrared (NIR) absorption and excellent photothermal conversion efficiency, which significantly enhanced the solar water evaporation performance of the hydrogel. Structurally, Ti_2O_3 exhibits a corundum-like crystal structure, which contributes to its thermal stability under the operational conditions. Then, the thermoelectric hydrogel (PVA/Fe(CN)$_6^{3-/4-}$) is placed on top of the photothermal hydrogel, generating a temperature difference to generate a voltage (Figure 1). The photothermal (PT, PTCX) and thermoelectric (PVA/Fe(CN)$_6^{3-/4-}$) hydrogels were synthesized according to the procedure detailed in Figure S1, using PVA as the structural matrix. Several different quantities of carbon-nanotube dispersions (0, 10, 20, and 30 mL) were incorporated into the PVA matrix, followed by the addition of GLA, Ti_2O_3, and HCl to form the hydrogels labeled PT, PTC10, PTC20, and PTC30, respectively. The scanning electron microscopy (SEM) images in Figure 2 show the microstructural morphology of the freeze-dried hydrogels and exhibit a porous structure across all samples.[27−29] The consistent structure suggests that adding Ti_2O_3 and CNT does not disrupt the inherent morphology of the hydrogel matrix. Moreover, the porous architecture facilitates capillary action, providing efficient pathways for water transport.[30] The particle size of ball-milled Ti_2O_3, approximately 500 nm, is shown in Figure S2a−c. This result indicates that Ti_2O_3 was successfully reduced to the nanoscale. The distribution of titanium elements was further confirmed using energy dispersive

https://doi.org/10.1021/acssuschemeng.4c10855
ACS Sustainable Chem. Eng. 2025, 13, 4231−4241

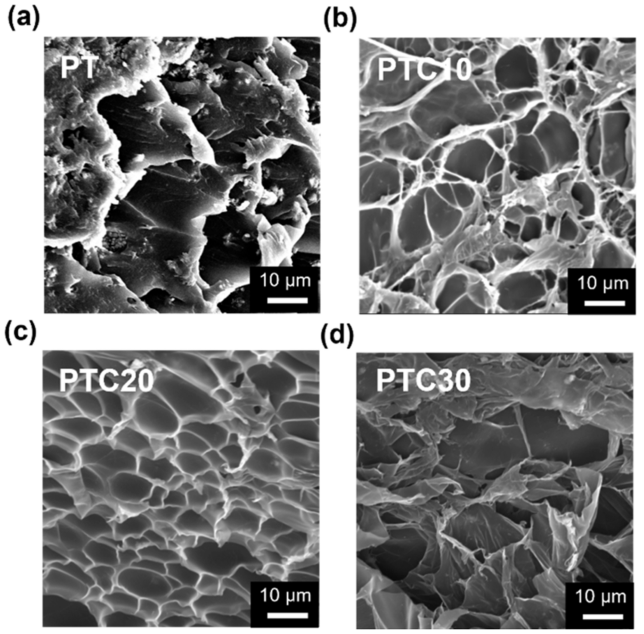

Figure 2. Morphological characterization of PT, PTCX hydrogels: SEM images of (a) PT, (b) PTC10, (c) PTC20, and (d) PTC30.

spectroscopy (EDS), see Figure S2d, which shows a uniform distribution.

The rheological test results in Figure 3a primarily indicate the elastic behavior of the PVA, PT, and PTCX hydrogels. The storage modulus (G') of all PVA, PT, and PTCX hydrogels is greater than the loss modulus (G'') over the 20 to 50 °C temperature range. This indicates that the hydrogels exhibit solid-like rather than liquid-like properties. These findings are significant for developing the device or thermoelectric devices in this study, as the hydrogel properties ensure stability even under temperature variations.[31,32] The mechanical properties of the PVA, PT, and PTCX hydrogels are assessed through tensile tests, as depicted in Figure 3b. The relatively low strain at break observed for the pure PVA hydrogel is primarily attributed to its intrinsically brittle network structure. This characteristic brittleness arises from several factors, including the relatively low molecular weight of the PVA used in this work (Mw: 31,000−50,000). Low molecular weight PVA tends to form a more rigid and less flexible network due to limited chain entanglement, which restricts polymer chain mobility and results in a lower capacity for elongation under tensile stress. The tensile strengths of PT, PTC10, PTC20, and PTC30 are higher than that of the pure PVA hydrogel, which indicates that including Ti_2O_3 and CNTs effectively strengthens the hydrogel structure. The increased proportion of CNTs decreases the overall PVA content. Although CNTs improve the mechanical properties, the negative impact of the reduced PVA content only slightly improves the mechanical properties. The results show that PT and PTCX hydrogels have better tensile strength and larger stretchability than that of pure PVA hydrogels. This enhancement is likely due to the uniform dispersion of Ti_2O_3 and CNTs within the network structure. The PT hydrogel sample showed the highest tensile strength (81.8 kPa), while PTC30 displayed the greatest elongation at break (17.8%).[33] The PT hydrogel exhibits the highest tensile strength due to the reinforcing effect of Ti_2O_3 nanoparticles, which enhance intermolecular interactions and restrict polymer chain mobility, thereby increasing the overall stiffness. In contrast, the nonmonotonic variation in tensile

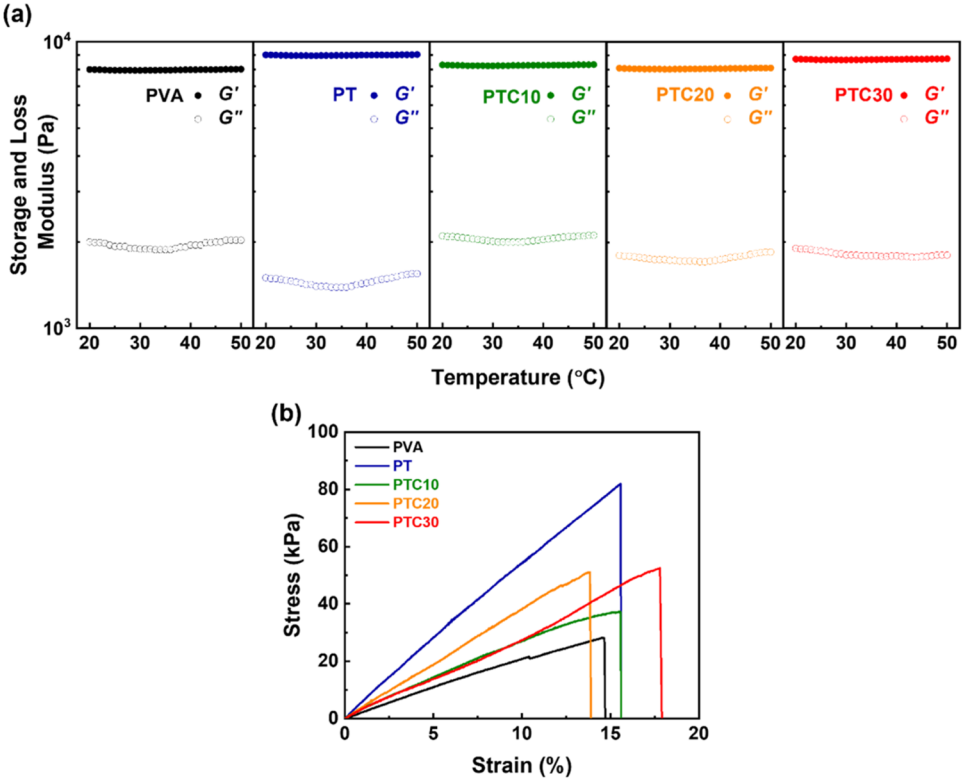

Figure 3. Mechanical properties of PVA, PT, PTCX hydrogels (a) Dynamic mechanical measurement of the storage modulus (G') and loss modulus (G'') of the hydrogels. (b) Tensile stress−strain curves of the hydrogels.

https://doi.org/10.1021/acssuschemeng.4c10855
ACS Sustainable Chem. Eng. 2025, 13, 4231−4241

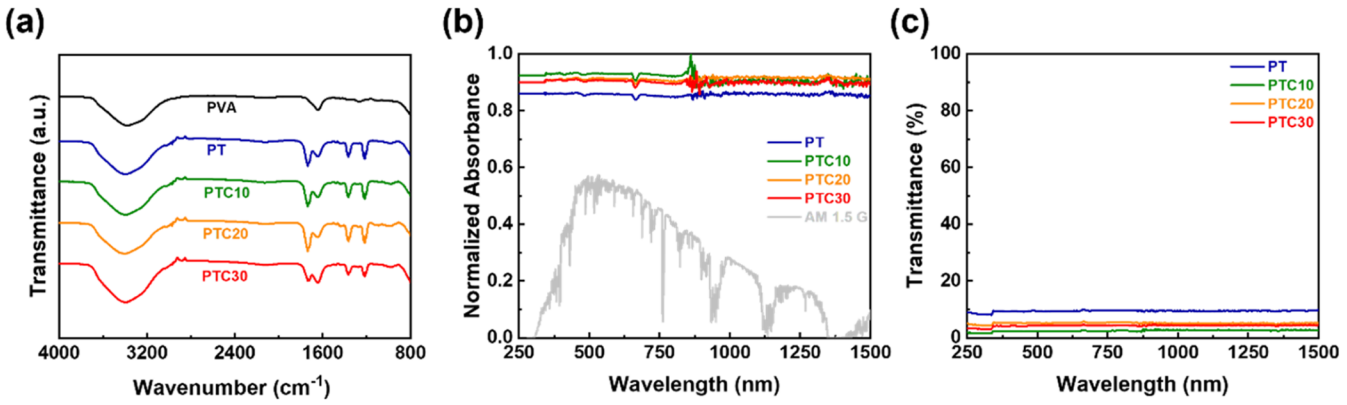

Figure 4. Characterization of PVA, PT, and PTCX hydrogels: (a) FTIR spectra of the hydrogels. (b) UV−vis-NIR spectra of the PT and PTCX hydrogels showing normalized absorbance curves. (c) UV−vis-NIR spectra of the PT and PTCX hydrogels showing transmittance curves.

properties with SWCNT content can be attributed to the balance between reinforcement and aggregation effects. The PCT30 hydrogel shows the longest fracture strain because CNTs introduce additional flexibility by acting as bridges between polymer chains, enhancing the elongation before rupture. Initially, adding CNTs enhances the mechanical strength and modulus by improving the network interactions. However, at higher concentrations, excessive aggregation reduces the stress transfer efficiency, leading to slight performance fluctuations. Also, we have conducted differential scanning calorimetry (DSC) analysis to determine the glass transition temperature (T_g) of the PVA hydrogel before and after the addition of Ti_2O_3 and CNTs (Figure S5). The results indicate that the incorporation of these nanomaterials leads to an increase in T_g, suggesting enhanced intermolecular interactions within the polymer matrix.

The chemical composition of the PVA, PT, and PTCX hydrogels was analyzed using Fourier transform infrared spectroscopy (FTIR) (Figure 4a), which reveals several prominent characteristic peaks at 3390, 1740, 1640, 1365, and 1220 cm^{-1}. The broad band around 3390 cm^{-1} corresponds to the O−H stretching, which is attributed to intermolecular and intramolecular hydrogen bonds. Notably, the addition of Ti_2O_3 and CNTs does not significantly shift these peaks, which indicates that these additives do not alter the intrinsic structure of the PVA hydrogel but rather disperse uniformly within the PVA network. The peak near 1740 cm^{-1} corresponds to C═O stretching, while the 1640 cm^{-1} peak correlates with C−O stretching in PVA. In addition, the peak at 1365 cm^{-1} is attributed to C−H bending, and the 1220 cm^{-1} peak is associated with symmetric C−C stretching or C−O stretching within the polymer backbone. The presence of these characteristic peaks in PVA indicates the presence of a PVA matrix.[34−36] X-ray diffraction (XRD) patterns further support the structural analysis, as shown in Figure S3a for Ti_2O_3 particles and Figure S3b−S3e for several hydrogels. The broad halos with sharp Ti_2O_3 peaks between 20 and 60° of PVA across all hydrogel samples confirm aggregation of PVA and dispersion of Ti_2O_3 in the hydrogels.[37] These results also indicate that Ti_2O_3 and CNTs did not change the structure of the PVA hydrogel.

The nanoscale structure of the hydrogel network is further clarified through small-angle X-ray scattering (SAXS) profiles of several different samples in the q-range from 0.001 to 0.7 $Å^{-1}$, as shown in Figure S4. The SAXS profile of the PVA hydrogel (Figure S4a) exhibits two distinct regions with different scattering slopes, which are divided by a turning point (between 0.01 and 0.02 $Å^{-1}$). Large-scale aggregates can be seen within the q-range of 0.001−0.01 $Å^{-1}$, while smaller aggregates appear in the 0.02−0.7 $Å^{-1}$ range. Also, all SAXS profiles show no noticeable difference at various temperatures, which implies that the microstructure of the hydrogels is stable and unaffected by temperature changes. The fractal structure of the PVA hydrogel can be analyzed at multiple scales using the Beaucage fitting model (Figure S4b). Scattering in the lower q-range (below 0.01 $Å^{-1}$) is predominantly influenced by contributions from global polymer clusters (Figure S4b) while scattering at q-values above 0.01 $Å^{-1}$ provides insight into the structure of the smaller building blocks that compose the global fractal structure (Figure S4e).[38−42] From the model fitting, the radius of gyration R_g for the clusters is estimated to be 1361 Å, while that for the smaller building blocks is approximately 128 Å. Figure S4c and S4d present SAXS profiles for the PT and PTC10 hydrogels, respectively, where adding Ti_2O_3 and CNT increases the scattering intensity significantly. The SAXS data indicate that Ti_2O_3 and the CNTs predominantly cause the scattering.

In order to evaluate the solar absorption capabilities, the light absorption and transmittance of the hydrogels were measured by using a UV−vis-NIR spectrophotometer. As illustrated in Figure 4b, all hydrogels showed excellent light absorption (about 80−90%) across the solar spectrum. PTC10 exhibits slightly higher absorption with minimal optical loss compared to the other samples. Furthermore, the hydrogels display low transmittance in the wavelength range 250−1500 nm, with PTC10 showing the lowest transmittance (Figure 4c).[43] A uniform dispersion of Ti_2O_3 and CNTs ensures effective photothermal energy conversion by providing consistent light absorption and heat generation. The observed results could be attributed to the ratio of Ti_2O_3 to CNTs. As the CNT content increases, the overall PVA ratio decreases, which decreases the hydrogel's cross-linking degree. This reduction in cross-linking affects the hydrogel's properties, including its light absorption. A high concentration of CNTs may impede the photothermal performance of Ti_2O_3, which suggests that an optimal ratio of these components is required. Despite only minor differences in absorption and transmittance among the PTCX hydrogels, their overall optical properties surpass those of the PT hydrogel.

The water evaporation performance experiments were conducted by using a 300 W Xe-lamp solar simulator. A thermal infrared camera was employed to capture and monitor

https://doi.org/10.1021/acssuschemeng.4c10855
ACS Sustainable Chem. Eng. 2025, 13, 4231−4241

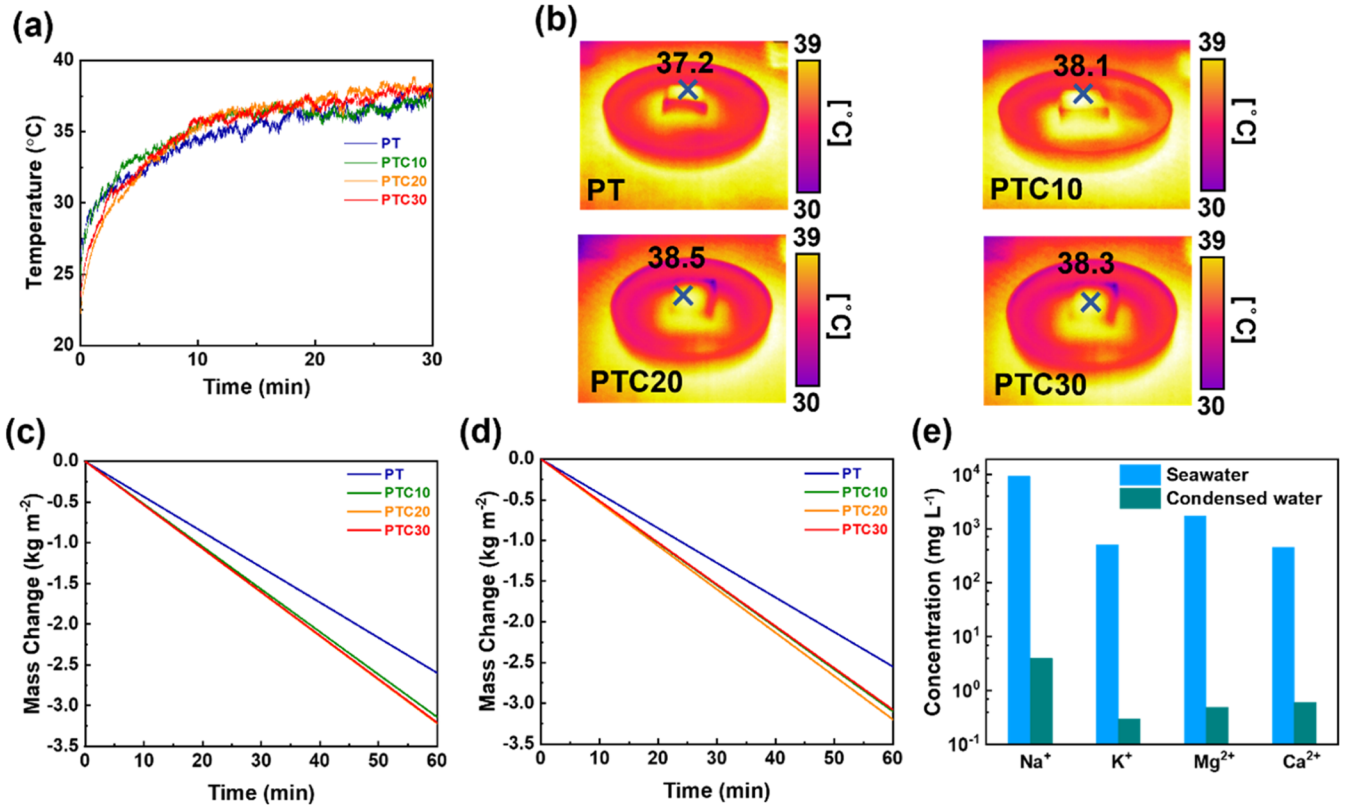

Figure 5. Photothermal properties of PT and PTCX hydrogels: (a) Temperature versus time under solar irradiation. (b) IR images capturing temperature changes during irradiation. (c) Pure water mass changes over time during evaporation. (d) Seawater mass changes over time during evaporation. (e) Concentrations of typical metal ions in seawater and condensed water after evaporation.

the temperature. The mass of the water loss was measured using a lab balance with a 0.1 mg resolution. All evaporation rates were measured after the system stabilized under one sun for 60 min. The photothermal behavior of the hydrogels under one sun (1 kW m^{-2}) illumination was investigated by monitoring the surface temperature with a thermal imaging camera. Within 20 min of exposure, the temperature of PTCX hydrogels increased from 22 °C to above 38 °C, while the PT hydrogel temperature only increased to 37.2 °C. The hydrogels containing CNTs (PTC10, PTC20, PTC30) showed slightly superior heating performance to those without CNTs (PT), see Figure 5a. Thermal images after 20 min of illumination (Figure 5b) clearly show the temperature difference between the hydrogels and the surrounding water. These results highlight their effective photothermal conversion capabilities. The ability of PT, PTC10, PTC20, and PTC30 to retain heat on their surfaces while minimizing energy loss to water indicates their photothermal capability.

Furthermore, the thermal conductivity was measured using the transient plane source (TPS) method. Although thermal conductivity slightly increased with increasing quantities of CNTs, it remained low (Table S1), which helped reduce heat loss to the surrounding water. Under one sun irradiation, the water evaporation rates were measured based on weight loss using an analytical balance. All hydrogels showed stable and linear evaporation rates (Figure 5c–d), with PTC30 reaching a pure water evaporation rate of 3.22 kg m^{-2} h^{-1} (Figure 5c). The evaporation rate is comparable to that reported in other studies.[44,45] The water flux for the hydrogels can be calculated from the measured evaporation rates. The water flux for pure PVA hydrogel is calculated to be 0.31 mL m^{-2} s^{-1}, while the water flux for PTC30 hydrogels is calculated to be 0.89 mL m^{-2} s^{-1}. The water fluxes calculated from evaporation rates indicate that the incorporation of these nanomaterials enhances photothermal conversion, improving the evaporation rate and preserving the original porous structure of the hydrogel. The practical feasibility of these hydrogels for seawater desalination was also demonstrated. During evaporation experiments using seawater, the hydrogels maintained their evaporation rates with no significant changes (Figure 5d). The concentration of ions such as Na^+, K^+, Mg^{2+}, and Ca^{2+} in the collected freshwater was reduced by three to 4 orders of magnitude (Figure 5e), i.e., it met the purity standards for drinking water set by the World Health Organization (WHO) and the U.S. Environmental Protection Agency (EPA).[46,47]

Subsequently, the thermoelectric properties of the PVA/$Fe(CN)_6^{3-/4-}$ hydrogel were measured. The ionic Seebeck coefficient is a key parameter to assess a material's thermoelectric (TE) performance. It quantifies the generated voltage based on a temperature gradient. The ionic Seebeck coefficient is defined as $S_i = -\Delta V/\Delta T$, where ΔT is the temperature difference across the hot and cold ends of the hydrogel, and ΔV denotes the resulting thermoelectric voltage that is generated when a temperature difference is applied.[48−55] The thermoelectric properties were evaluated using a custom-built measurement system under high relative humidity (RH ∼ 70%). In the PVA/$Fe(CN)_6^{3-/4-}$ hydrogel, the thermogalvanic effect is driven by the temperature-dependent electrochemical reaction of the redox couple, specifically $Fe(CN)_6^{3-} + e^- \rightleftharpoons Fe(CN)_6^{4-}$. The transfer of electrons in this redox process creates a potential difference between the hot and cold regions of the electrolyte.[56]

https://doi.org/10.1021/acssuschemeng.4c10855
ACS Sustainable Chem. Eng. 2025, 13, 4231−4241

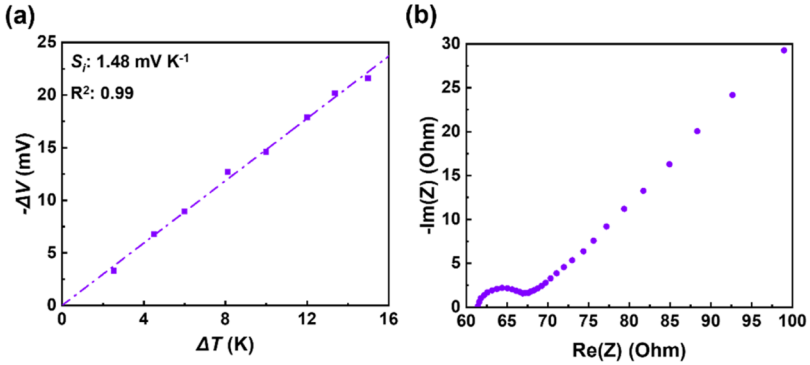

Figure 6. Thermoelectric properties of PVA/$Fe(CN)_6^{3-/4-}$ thermoelectric hydrogel: (a) $-\Delta V-\Delta T$ curve, where the slope represents the Seebeck coefficient. (b) EIS spectra, where the intercept can be used to calculate the ionic conductivity using the formula.

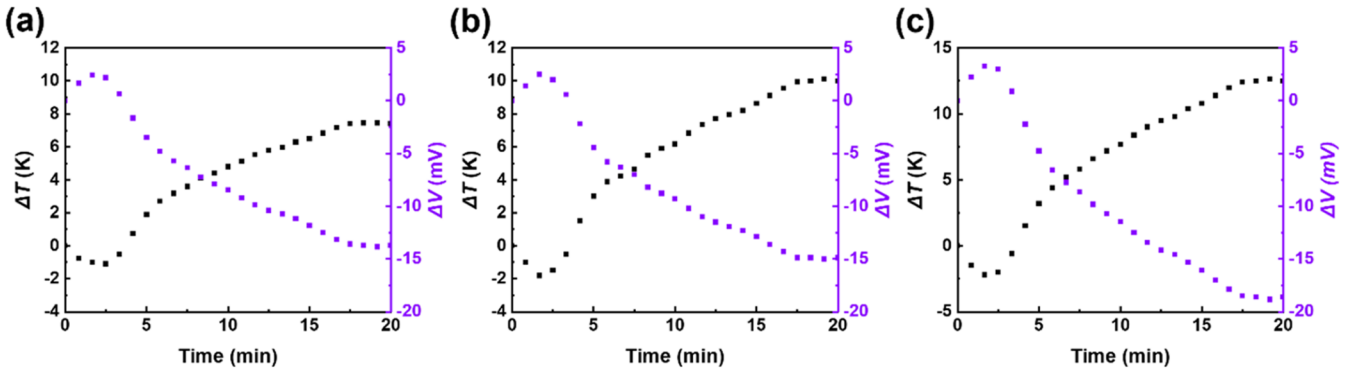

Figure 7. ΔT and corresponding ΔV under various solar irradiation intensities: (a) 0.8 kW m^{-2}, (b) 1.0 kW m^{-2}, and (c) 1.2 kW m^{-2}.

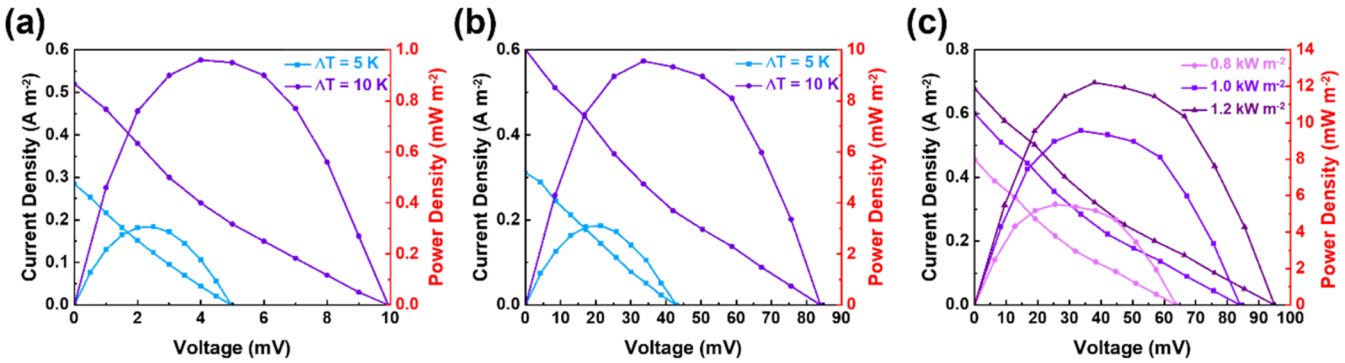

Figure 8. Current−voltage and power density−voltage characteristics of the thermoelectric PVA-based hydrogel of (a) 1 unit, (b) 9 units in various ΔT, and (c) 9 units under various solar irradiation intensities.

In contrast, the accompanying ion-concentration difference from the redox reaction facilitates ion migration across the electrodes.[57,58] This continuous flow of electrons and ions enables steady power generation in the hydrogel-based TGC.[59−62] The relationship between ΔV and ΔT for the hydrogel sample is shown in Figure 6a, from which S_i can be derived (1.48 mV K^{-1}) based on the slope of the curve. The ionic conductivity (σ_i) was measured using AC impedance spectroscopy across a frequency range of 1 Hz to 1 MHz at ambient conditions. The value of σ_i was calculated using the formula $\sigma_i = d/(A \times R)$, where A is the cross-sectional area, R denotes the bulk resistance, and d signifies the sample thickness.[63,64] The results (Figure 6b) indicate the hydrogel's moderately high ionic conductivity, calculated as 25.51 mS cm^{-1}. This high ionic conductivity is essential for efficient ion transport and an enhanced thermoelectric performance.

The low-grade solar waste heat generated by PT and PTCX hydrogels provides a sustainable and cost-effective method for producing thermoelectric via the Seebeck effect.[65] We then measured the photothermal and thermoelectric properties of a single hydrogel under illumination. Here, the thermoelectric hydrogel was placed on top of the photothermal hydrogel to harness the energy. The design positions the hot end at the bottom and the cold end at the top with aluminum foil attached to nickel foil to reflect sunlight and reduce the temperature of the upper surface. This arrangement increased the temperature gradient between the hot and cold ends—see Figure 1. Figure 7 presents the ΔT and ΔV versus time curves of a single thermoelectric hydrogel cell with a size of about 1 × 1 × 1 cm^3 under varying solar irradiation intensities. When exposed to 1 kW m^{-2} solar illumination, ΔT increased to 10 K after about 20 min, while the generated ΔV reached 15 mV.

https://doi.org/10.1021/acssuschemeng.4c10855
ACS Sustainable Chem. Eng. 2025, 13, 4231−4241

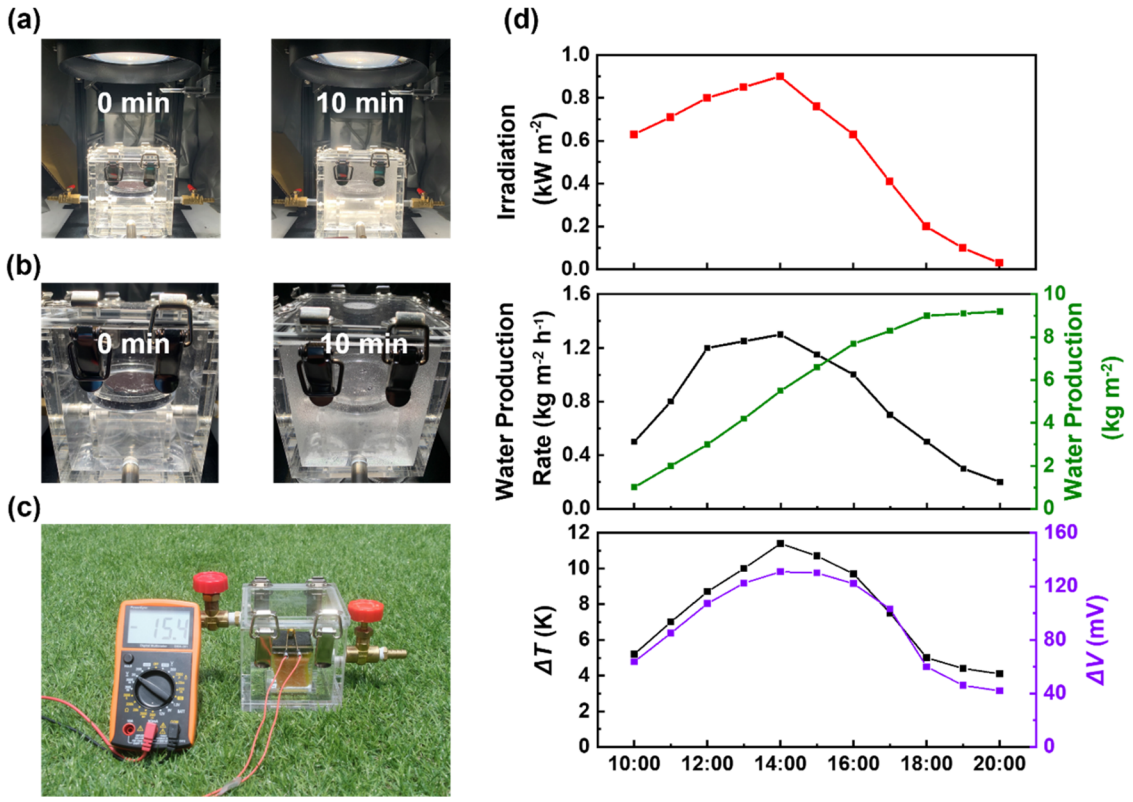

Figure 9. (a–b) Images illustrating the formation process of vapor and condensed water droplets after 10 min of irradiation. (c) Image of the self-assembled outdoor solar evaporation setup. (d) Variation of solar intensity, changes in water production rate and total volume, ΔT and ΔV generated during the 10 h period.

When exposed to 0.8 kW m^{-2} solar illumination, ΔT increased to 7 K, while the generated ΔV reached 12 mV. When exposed to 1.2 kW m^{-2} solar illumination, ΔT increased to 13 K, while the generated ΔV reached 18 mV. As the light intensity increases, the temperature difference and voltage follow a corresponding rising trend. All voltages generated under various solar irradiation intensities were consistent with the theoretical Seebeck coefficient. This observation highlights the hydrogel system's responsiveness to solar irradiation, which makes it a promising candidate for low-grade waste heat recovery and thermoelectric energy generation.

The current density-power density–voltage characteristics are measured to further clarify the output power of a single thermoelectric hydrogel and connected 9 units in series. As shown in Figure 8a, a single thermoelectric hydrogel at a ΔV of 5 K generates an open-circuit voltage of approximately 5 mV, with a current density of about 0.3 A m^{-2} and a maximum power density of 0.3 mW m^{-2}. When the temperature difference increased to 10 K, the open-circuit voltage rose to about 10 mV, the current density increased to about 0.5 A m^{-2}, and the maximum power density approached 1 mW m^{-2}. Figure 8b shows the $I-V$ and $P-V$ curves for nine thermoelectric hydrogels connected in series. Platinum sheet electrodes were attached to nickel foil, which connected multiple thermoelectric hydrogels in series. For an ΔT of 5 K, the open-circuit voltage rose significantly (to about 45 mV), with a current density of approximately 0.3 A m^{-2} and a maximum power density close to 3 mW m^{-2}. When the temperature difference was increased to 10 K, the open-circuit voltage reached about 85 mV, the current density increased to about 0.6 A m^{-2}, and the maximum power density reached approximately 9.6 mW m^{-2}. These results demonstrate that with increasing series connections, both the open-circuit voltage and power density improve, which confirms the scalability of the system. Figure 8c illustrates that the data obtained from the thermoelectric hydrogels in series exhibit a positive correlation with increasing solar intensity, which indicates the effectiveness of the system in harnessing solar energy for thermoelectric power generation. The measured output voltages in Figure 8c are consistent with the theoretical values for different solar irradiation intensities. This scalable approach reveals a significant potential for practical applications for sustainable energy solutions, especially when it comes to utilizing low-grade solar waste heat.

The low-grade solar heat generated by the PTCX hydrogels is a sustainable and cost-effective approach to energy production. The solar-driven thermoelectric hydrogels were positioned on top of the PTC10 hydrogels in a custom-made device to harness thermoelectric energy through the Seebeck effect. The setup includes an inner box, which holds seawater and the photothermal PTC10 hydrogel (dimensions 5 × 5 × 1 cm^3), and an outer box that collects the condensed pure water after evaporation. Figure 9a,b illustrates that a significant amount of water vapor was generated within only 10 min of sunlight exposure, with the condensed water effectively collected using the device. An outdoor solar evaporation test assessed the device's effectiveness in more detail. The device was placed outdoors, and the thermoelectric hydrogels were connected to a multimeter to record data, as shown in Figure 9c. The test was conducted from 10 AM to 6 PM in July 2024 in the courtyard of the College of Engineering at National Taiwan University, Taipei. The solar intensity fluctuated

https://doi.org/10.1021/acssuschemeng.4c10855
ACS Sustainable Chem. Eng. 2025, 13, 4231–4241

throughout the day and peaked at 0.9 kW m^{-2} at 2 PM, as shown in Figure 9d. At the same time, the water production rate peaked at 1.3 kg m^{-2} h^{-1}, with a total water yield of 9.2 kg m^{-2} over the 10 h. This output was sufficient to provide about 10 L of freshwater, which is the daily need of four adults. Simultaneously, the temperature difference and voltage output of the solar-driven thermoelectric (PVA/$Fe(CN)_6^{3-/4-}$) hydrogels were measured. At 2 PM, the temperature difference reached approximately 11 K, generating a voltage of 130 mV from 9 solar-driven thermoelectric hydrogels connected in series. Video S1 shows a stable voltage output between 1 and 2 PM, which confirms the device is reliable. Overall, the device has demonstrated excellent long-term stability in a 10-h outdoor test. In addition, the device could connect nine thermoelectric hydrogels in series and generate electrical energy that can potentially be used for low-power-driven electronic devices. To maintain long-term stability, it is essential to effectively sustain water evaporation efficiency and thermoelectric voltage stability. The Ti_2O_3 nanoparticles and CNTs in the photothermal hydrogels exhibit high solar absorption and thermal stability, ensuring continuous and efficient heat generation for prolonged water evaporation. The hydrophilic and porous structure of the PVA-based hydrogel ensures stable water transport, preventing dehydration and maintaining continuous evaporation. Furthermore, the cross-linked network of the hydrogels prevents material degradation during long-term operation, providing structural stability and minimizing deformation. The hydrogel structure also prevents salt accumulation, ensuring that seawater impurities do not affect the long-term performance. This hydrogel-based system offers a practical and environmentally friendly approach by combining solar desalination with thermoelectric energy generation. As a result, it is highly suitable for off-grid and remote areas.

CONCLUSIONS

By combining thermoelectric hydrogels with photothermal hydrogels, we succeeded in developing a device capable of simultaneously generating both freshwater and electricity. The PTCX hydrogel exhibited exceptional light absorption and efficient photothermal conversion with a notable water evaporation rate of 3.22 kg m^{-2} h^{-1}. Moreover, the porous structure of the hydrogel effectively removes ions from seawater. When combined with thermoelectric hydrogels, the self-made acrylic device achieved a power density of 9.6 mW m^{-2} under solar irradiation. Outdoor testing confirmed the device's ability to produce 9.2 kg m^{-2} of water and maintain a stable voltage output of 130 mV over 10 h. Overall, this combined system presents a sustainable solution for remote regions with limited access to freshwater and electricity. It offers the potential to significantly improve resource availability while reducing reliance on traditional, environmentally harmful energy sources.

EXPERIMENTAL SECTION

Materials. Poly(vinyl alcohol) (PVA) with an average molecular weight (M_w) of 31,000−50,000 and a degree of hydrolysis of 87−89%, hydrochloric acid (HCl, 37 wt %), dititanium trioxide (Ti_2O_3 powders, 100 mesh), glutaraldehyde (GLA, 25 wt % aqueous solution), potassium hexacyanidoferrate(II) ($K_4[Fe(CN)_6]\cdot 3H_2O$), and potassium ferricyanide ($K_3[Fe(CN)_6]$) were procured from Sigma-Aldrich. Single-walled carbon nanotubes (SWCNTs) (with a diameter of less than 2 nm, a length greater than 5 μm, and 80% purity) and polyvinylpyrrolidone (PVP) were sourced from Tuball. All chemicals were used as received without further purification

Preparation and Characterization of Photothermal Composite Hydrogel. The PVA/Ti_2O_3/CNTs (PTC) hydrogels were synthesized according to the procedure illustrated in Figure S1. Initially, SWCNTs and polyvinylpyrrolidone (PVP) are dispersed in deionized (DI) water at a 10:1 ratio to form a CNT dispersion via tip sonication. In a separate step, 1.25 g of PVA and 280 μL of GLA are added to 10 mL of DI water along with 10, 20, or 30 mL of the SWCNT dispersion (1 mg mL^{-1}). The mixture was heated and stirred until PVA is fully dissolved. Ti_2O_3 powder is ball-milled into nanoparticles, which Ti_2O_3 was added to DI water at a concentration of 0.5 g mL^{-1} to perform wet ball milling. The particle size of the ball-milled Ti_2O_3, approximately 500 nm, is shown in Figure S2a−c. This result indicates that Ti_2O_3 was successfully reduced to the nanoscale. Once the dissolution of PVA is complete, 300 μL (0.15 g) of Ti_2O_3 is introduced, and stirring is continued. To initiate cross-linking, 750 μL of diluted hydrochloric acid (HCl, 3.5 wt %) is added, and the solution is stirred thoroughly. The resulting mixture is then poured into molds to allow gelation. After the gelation process, the hydrogels are rinsed with DI water and subjected to a freeze−thaw cycle. The gels are washed again with DI water after the freeze−thaw process. The final hydrogels are designated as PT, PTC10, PTC20, and PTC30, respectively, based on the volume of the SWCNT dispersion used.

Preparation and Characterization of Thermoelectric Hydrogel. To prepare the thermoelectric hydrogel, 0.42 M $K_4[Fe(CN)_6]\cdot 3H_2O$ and 0.25 M $K_3[Fe(CN)_6]$ are dissolved in DI water. Separately, 1.25 g of PVA and 280 μL of GLA were dissolved in 10 mL of DI water, heating, and stirring until the PVA is fully dissolved. Once dissolution is complete, add 750 μL of diluted HCl (3.5 wt %) and stir thoroughly to initiate cross-linking. The resulting mixture is then poured into molds to allow gelation. After gelation, the gels were rinsed with DI water, followed by freeze-drying, and they were washed again with DI water to obtain the final hydrogel. The prepared hydrogel is subsequently soaked in $K_4[Fe(CN)_6]/K_3[Fe(CN)_6]$ aqueous solution, as depicted in Figure S1.

Fabrication of Dual-Function Photothermal and Thermoelectric Device. To fabricate the device, a PTC10 hydrogel (5 × 5 × 1 cm^3) is placed within the inner layer of an acrylic housing as the base layer. On top of the PTC10 hydrogel, 9 thermoelectric hydrogels with a size of 1 × 1 × 1 cm^3 are stacked and connected in series using nickel foil for effective electrical continuity. Platinum sheets are used as electrodes, while aluminum foil is applied to the top electrode of the thermoelectric hydrogels to reflect sunlight and enhance the temperature gradient across the hydrogels. For optimal thermal conduction, thermally conductive tape is used to securely fasten the series-connected thermoelectric generators (TEGs) to the PTC10 hydrogel.

ASSOCIATED CONTENT

Supporting Information

The Supporting Information is available free of charge at https://pubs.acs.org/doi/10.1021/acssuschemeng.4c10855.

Characterization of various techniques, thermal conductivity of hydrogels, schematic of preparation of hydrogels, the SEM images at different magnifications of Ti_2O_3 nanoparticles, X-ray diffraction of Ti_2O_3 nanoparticles powder and hydrogels, SAXS analysis of hydrogels and schematic diagram of the hydrogel network, and differential scanning calorimetry (DSC) analysis of hydrogels (PDF)

Stable voltage output between 1 and 2 PM (MP4)

https://doi.org/10.1021/acssuschemeng.4c10855
ACS Sustainable Chem. Eng. 2025, 13, 4231−4241

AUTHOR INFORMATION

Corresponding Author

Cheng-Liang Liu − *Department of Materials Science and Engineering, National Taiwan University, Taipei 10617, Taiwan; Institute of Polymer Science and Engineering and Advanced Research Center for Green Materials Science and Technology, National Taiwan University, Taipei 10617, Taiwan;* orcid.org/0000-0002-8778-5386; Email: liucl@ntu.edu.tw

Authors

Yu-Hao Wang − *Department of Materials Science and Engineering, National Taiwan University, Taipei 10617, Taiwan*

Ching-Chieh Hsu − *Department of Materials Science and Engineering, National Taiwan University, Taipei 10617, Taiwan*

Shao-Huan Hong − *Department of Materials Science and Engineering, National Taiwan University, Taipei 10617, Taiwan*

Jian-Fa Ding − *Department of Materials Science and Engineering, National Taiwan University, Taipei 10617, Taiwan*

U-Ser Jeng − *National Synchrotron Radiation Research Center, Hsinchu 30076, Taiwan;* orcid.org/0000-0002-2247-5061

Dun-Yen Kang − *Department of Chemical Engineering, National Taiwan University, Taipei 10617, Taiwan;* orcid.org/0000-0002-2349-4432

Shyh-Chyang Luo − *Department of Materials Science and Engineering, National Taiwan University, Taipei 10617, Taiwan; Institute of Polymer Science and Engineering, National Taiwan University, Taipei 10617, Taiwan;* orcid.org/0000-0003-3972-1086

Shih-Huang Tung − *Department of Materials Science and Engineering, National Taiwan University, Taipei 10617, Taiwan; Institute of Polymer Science and Engineering, National Taiwan University, Taipei 10617, Taiwan;* orcid.org/0000-0002-6787-4955

Complete contact information is available at: https://pubs.acs.org/10.1021/acssuschemeng.4c10855

Notes

The authors declare no competing financial interest.

ACKNOWLEDGMENTS

The authors acknowledge support from the 2030 Cross-Generation Young Scholars Program funded by the National Science and Technology Council (NSTC) in Taiwan (NSTC 113-2628-E-002-009 and 113-2124-M-002-010), the Academic Research−Career Development Project (Sprout Research Projects) funded by the National Taiwan University (NTU113L7839), and the Advanced Research Center for Green Materials Science and Technology under the Featured Area Research Center Program, as part of the Higher Education Sprout Project by the Ministry of Education (113L9006). The authors thank the National Synchrotron Radiation Research Center (NSRRC) of Taiwan for providing beamline TPS 13A1. TOC graphics and figures were created by biorender.com.

REFERENCES

(1) Xu, Y.; Guo, Z.; Wang, J.; Chen, Z.; Yin, J.; Zhang, Z.; Huang, J.; Qian, J.; Wang, X. Harvesting Solar Energy by Flowerlike Carbon Cloth Nanocomposites for Simultaneous Generation of Clean Water and Electricity. *ACS Appl. Mater. Interfaces* **2021**, *13*, 27129−27139.

(2) Chen, C.; Kuang, Y.; Hu, L. Challenges and Opportunities for Solar Evaporation. *Joule* **2019**, *3*, 683−718.

(3) Vorosmarty, C. J.; Green, P.; Salisbury, J.; Lammers, R. B. Global water resources: vulnerability from climate change and population growth. *Science* **2000**, *289*, 284−288.

(4) Liao, X.; Chai, L.; Jiang, Y.; Ji, J.; Zhao, X. Inter-provincial electricity transmissions' co-benefit of national water savings in China. *J. Cleaner Prod.* **2019**, *229*, 350−357.

(5) Hong, M.; Lyv, W.; Li, M.; Xu, S.; Sun, Q.; Zou, J.; Chen, Z.-G. Rashba Effect Maximizes Thermoelectric Performance of GeTe Derivatives. *Joule* **2020**, *4*, 2030−2043.

(6) Gong, J.; Li, C.; Wasielewski, M. R. Advances in solar energy conversion. *Chem. Soc. Rev.* **2019**, *48*, 1862−1864.

(7) Zhu, L.; Ding, T.; Gao, M.; Peh, C. K. N.; Ho, G. W. Shape conformal and thermal insulative organic solar absorber sponge for photothermal water evaporation and thermoelectric power generation. *Adv. Energy Mater.* **2019**, *9*, No. 1900250.

(8) Ren, J.; Ding, Y.; Gong, J.; Qu, J.; Niu, R. Simultaneous Solar-driven Steam and Electricity Generation by Cost-effective, Easy Scale-up MnO2-based Flexible Membranes. *Energy Environ. Mater.* **2023**, *6*, No. e12376.

(9) Lin, Y.-H.; Lin, H.-H.; Lee, Y.-S.; Yu, W.-Y.; Luo, S.-C.; Kang, D.-Y. MOF-303 with lowered water evaporation enthalpy for solar steam generation. *ACS Appl. Mater. Interfaces* **2024**, *16*, 49640−49650.

(10) Curto, D.; Franzitta, V.; Guercio, A. A review of the water desalination technologies. *Appl. Sci.* **2021**, *11*, 670.

(11) Li, J.; Wei, W.; Chen, Y.; Liu, Z. Multiple Sites Organic Small-Molecule Electrode Material for High-Capacity Seawater Desalination. *ACS Sustainable Chem. Eng.* **2024**, *12*, 16388.

(12) Perumal, S.; Samanta, M.; Ghosh, T.; Shenoy, U. S.; Bohra, A. K.; Bhattacharya, S.; Singh, A.; Waghmare, U. V.; Biswas, K. Realization of high thermoelectric figure of merit in GeTe by complementary co-doping of Bi and In. *Joule* **2019**, *3*, 2565−2580.

(13) Luo, Y.; Cai, S.; Hao, S.; Pielnhofer, F.; Hadar, I.; Luo, Z.-Z.; Xu, J.; Wolverton, C.; Dravid, V. P.; Pfitzner, A.; et al. High-performance thermoelectrics from cellular nanostructured Sb2Si2Te6. *Joule* **2020**, *4*, 159−175.

(14) Cheng, H.; Le, Q.; Liu, Z.; Qian, Q.; Zhao, Y.; Ouyang, J. Ionic thermoelectrics: principles, materials and applications. *J. Mater. Chem. C* **2022**, *10*, 433−450.

(15) Zhao, D.; Würger, A.; Crispin, X. Ionic thermoelectric materials and devices. *J. Energy Chem.* **2021**, *61*, 88−103.

(16) Liu, Y.; Cui, M.; Ling, W.; Cheng, L.; Lei, H.; Li, W.; Huang, Y. Thermo-electrochemical cells for heat to electricity conversion: from mechanisms, materials, strategies to applications. *Energy Environ. Sci.* **2022**, *15*, 3670−3687.

(17) Zhou, H.; Inoue, H.; Ujita, M.; Yamada, T. Advancement of electrochemical thermoelectric conversion with molecular technology. *Angew. Chem., Int. Ed.* **2023**, *135*, No. e202213449.

(18) Lee, L. C.; Huang, K. T.; Lin, Y. T.; Jeng, U. S.; Wang, C. H.; Tung, S. H.; Huang, C. J.; Liu, C. L. A pH-Sensitive Stretchable Zwitterionic Hydrogel with Bipolar Thermoelectricity. *Small* **2024**, *20*, No. 2311811.

(19) Sharshir, S. W.; Algazzar, A. M.; Elmaadawy, K. A.; Kandeal, A. W.; Elkadeem, M. R.; Arunkumar, T.; Zang, J.; Yang, N. New hydrogel materials for improving solar water evaporation, desalination and wastewater treatment: A review. *Desalination* **2020**, *491*, No. 114564.

(20) Kaviti, A. K.; Balaji, J. S. G.; Ram, A. S.; Kumari, A. A. An overview on hydrogel materials for solar desalination. *Mater. Today: Proc.* **2021**, *44*, 2526−2532.

(21) Salehi, A. A.; Ghannadi-Maragheh, M.; Torab-Mostaedi, M.; Torkaman, R.; Asadollahzadeh, M. Hydrogel materials as an emerging

platform for desalination and the production of purified water. *Sep. Purif. Rev.* **2021**, *50*, 380−399.
(22) Wu, Y. C.; Wang, H. M.; Yuan, L. L.; Zhang, Q. Q.; Liu, Y. Q.; Shao, C. Y.; Hou, Q. X.; Sun, R. C. Lignin-Based Functional Hydrogels: An Eco-friendly Bulk Material. *ACS Sustainable Chem. Eng.* **2024**, *12*, 17952.
(23) Guo, Y.; Lu, H.; Zhao, F.; Zhou, X.; Shi, W.; Yu, G. Biomass-derived hybrid hydrogel evaporators for cost-effective solar water purification. *Adv. Mater.* **2020**, *32*, No. 1907061.
(24) Yang, P.; Liu, K.; Chen, Q.; Li, J.; Duan, J.; Xue, G.; Xu, Z.; Xie, W.; Zhou, J. Solar-driven simultaneous steam production and electricity generation from salinity. *Energy Environ. Sci.* **2017**, *10*, 1923−1927.
(25) Ren, J.; Chen, L.; Gong, J.; Qu, J.; Niu, R. Hofmeister effect mediated hydrogel evaporator for simultaneous solar evaporation and thermoelectric power generation. *Chem. Eng. J.* **2023**, *458*, No. 141511.
(26) Mu, X.; Zhou, J.; Wang, P.; Chen, H.; Yang, T.; Chen, S.; Miao, L.; Mori, T. A robust starch−polyacrylamide hydrogel with scavenging energy harvesting capacity for efficient solar thermo-electricity−freshwater cogeneration. *Energy Environ. Sci.* **2022**, *15*, 3388−3399.
(27) Jiang, S.; Liu, S.; Feng, W. PVA hydrogel properties for biomedical application. *J. Mech. Behav. Biomed. Mater.* **2011**, *4*, 1228−1233.
(28) Lin, M.-H.; Hong, S.-H.; Ding, J.-F.; Liu, C.-L. Organic Porous Materials and Their Nanohybrids for Next-Generation Thermo-electric Application. *ACS Appl. Mater. Interfaces* **2024**, *16*, 67116.
(29) Hsiao, Y.-C.; Lee, L.-C.; Lin, Y.-T.; Hong, S.-H.; Wang, K.-C.; Tung, S.-H.; Liu, C.-L. Stretchable polyvinyl alcohol and sodium alginate double network ionic hydrogels for low-grade heat harvesting with ultrahigh thermopower. *Mater. Today Energy* **2023**, *37*, No. 101383.
(30) Guo, Y.; Zhou, X.; Zhao, F.; Bae, J.; Rosenberger, B.; Yu, G. Synergistic energy nanoconfinement and water activation in hydrogels for efficient solar water desalination. *ACS Nano* **2019**, *13*, 7913−7919.
(31) Chen, Q.; Cheng, B.; Wang, Z.; Sun, X.; Liu, Y.; Sun, H.; Li, J.; Chen, L.; Zhu, X.; Huang, L.; et al. Rarely negative-thermovoltage cellulose ionogel with simultaneously boosted mechanical strength and ionic conductivity via ion-molecular engineering. *J. Mater. Chem. A* **2023**, *11*, 2145−2154.
(32) Villar-Chavero, M. M.; Domínguez, J. C.; Alonso, M. V.; Oliet, M.; Rodriguez, F. Tuning the rheological properties of cellulosic ionogels reinforced with chitosan: The role of the deacetylation degree. *Carbohydr. Polym.* **2019**, *207*, 775−781.
(33) Souri, H.; Banerjee, H.; Jusufi, A.; Radacsi, N.; Stokes, A. A.; Park, I.; Sitti, M.; Amjadi, M. Wearable and stretchable strain sensors: materials, sensing mechanisms, and applications. *Adv. Intell. Syst.* **2020**, *2*, No. 2000039.
(34) Mansur, H. S.; Sadahira, C. M.; Souza, A. N.; Mansur, A. A. P. FTIR spectroscopy characterization of poly (vinyl alcohol) hydrogel with different hydrolysis degree and chemically crosslinked with glutaraldehyde. *Mater. Sci. Eng.: C* **2008**, *28*, 539−548.
(35) Chen, Q.; Chen, B.; Xiao, S.; Feng, J.; Yang, J.; Yue, Q.; Zhang, X.; Wang, T. Giant thermopower of hydrogen ion enhanced by a strong hydrogen bond system. *ACS Appl. Mater. Interfaces* **2022**, *14*, 19304−19314.
(36) Chen, B.; Chen, Q.; Xiao, S.; Feng, J.; Zhang, X.; Wang, T. Giant negative thermopower of ionic hydrogel by synergistic coordination and hydration interactions. *Sci. Adv.* **2021**, *7*, No. eabi7233.
(37) Ricciardi, R.; Auriemma, F.; De Rosa, C.; Lauprêtre, F. X-ray diffraction analysis of poly (vinyl alcohol) hydrogels, obtained by freezing and thawing techniques. *Macromolecules* **2004**, *37*, 1921−1927.
(38) Zhao, D.; Wang, H.; Khan, Z. U.; Chen, J.; Gabrielsson, R.; Jonsson, M. P.; Berggren, M.; Crispin, X. Ionic thermoelectric supercapacitors. *Energy Environ. Sci.* **2016**, *9*, 1450−1457.
(39) Park, S.; Kim, B.; Cho, C.; Kim, E. Mesogenic polymer composites for temperature-programmable thermoelectric ionogels. *J. Mater. Chem. A* **2022**, *10*, 13958−13968.
(40) Hong, S.; Zou, G.; Kim, H.; Huang, D.; Wang, P.; Alshareef, H. N. Photothermoelectric response of Ti3C2T x MXene confined ion channels. *ACS Nano* **2020**, *14*, 9042−9049.
(41) Lin, Y.-T.; Hsu, C.-C.; Hong, S.-H.; Lee, L.-C.; Jeng, U. S.; Chen, H.-L.; Tung, S.-H.; Liu, C.-L. Highly conductive triple network hydrogel thermoelectrochemical cells with low-grade heat harvesting. *J. Power Sources* **2024**, *609*, No. 234647.
(42) Lee, C.-Y.; Lin, Y.-T.; Hong, S.-H.; Wang, C.-H.; Jeng, U. S.; Tung, S.-H.; Liu, C.-L. Mixed Ionic−Electronic Conducting Hydrogels with Carboxylated Carbon Nanotubes for High Performance Wearable Thermoelectric Harvesters. *ACS Appl. Mater. Interfaces* **2023**, *15*, 56072−56083.
(43) Lei, W.; Liu, Y.; Khan, S.; Suzuki, N.; Terashima, C.; Fujishima, A.; Liu, M. Synergistically regulated surface structure and water transportation of sponge hydrogel evaporator for efficient water desalination. *Desalination* **2022**, *533*, No. 115780.
(44) Zhou, X.; Zhao, F.; Guo, Y.; Zhang, Y.; Yu, G. A hydrogel-based antifouling solar evaporator for highly efficient water desalination. *Energy Environ. Sci.* **2018**, *11*, 1985−1992.
(45) Deng, Z.; Miao, L.; Liu, P.-F.; Zhou, J.; Wang, P.; Gu, Y.; Wang, X.; Cai, H.; Sun, L.; Tanemura, S. Extremely high water-production created by a nanoink-stained PVA evaporator with embossment structure. *Nano Energy* **2019**, *55*, 368−376.
(46) Qi, H.; Wei, T.; Zhao, W.; Zhu, B.; Liu, G.; Wang, P.; Lin, Z.; Wang, X.; Li, X.; Zhang, X.; Zhu, J. An Interfacial Solar-Driven Atmospheric Water Generator Based on a Liquid Sorbent with Simultaneous Adsorption−Desorption. *Adv. Mater.* **2019**, *31*, No. 1903378.
(47) Surwade, S. P.; Smirnov, S. N.; Vlassiouk, I. V.; Unocic, R. R.; Veith, G. M.; Dai, S.; Mahurin, S. M. Water desalination using nanoporous single-layer graphene. *Nat. Nanotechnol.* **2015**, *10*, 459−464.
(48) Jiang, Q.; Sun, H.; Zhao, D.; Zhang, F.; Hu, D.; Jiao, F.; Qin, L.; Linseis, V.; Fabiano, S.; Crispin, X.; et al. High Thermoelectric Performance in n-Type Perylene Bisimide Induced by the Soret Effect. *Adv. Mater.* **2020**, *32*, No. 2002752.
(49) Guan, X.; Cheng, H.; Ouyang, J. Significant enhancement in the Seebeck coefficient and power factor of thermoelectric polymers by the Soret effect of polyelectrolytes. *J. Mater. Chem. A* **2018**, *6*, 19347−19352.
(50) Sun, S.; Li, M.; Shi, X. L.; Chen, Z. G. Advances in ionic thermoelectrics: from materials to devices. *Adv. Energy Mater.* **2023**, *13*, No. 2203692.
(51) Zhang, C.; Shi, X. L.; Liu, Q.; Chen, Z. G. Hydrogel-Based Functional Materials for Thermoelectric Applications: Progress and Perspectives. *Adv. Funct. Mater.* **2024**, *34*, No. 2410127.
(52) Pai, Y. H.; Tang, J.; Zhao, Y.; Liang, Z. Ionic organic thermoelectrics with impressively high thermopower for sensitive heat harvesting scenarios. *Adv. Energy Mater.* **2023**, *13*, No. 2202507.
(53) Pai, Y. H.; Xu, C.; Zhu, R.; Ding, X.; Bai, S.; Liang, Z.; Chen, L. Piezoelectric-Augmented Thermoelectric Ionogels for Self-Powered Multimodal Medical Sensors. *Adv. Mater.* **2025**, *37*, No. 2414663.
(54) Wei, S.; Ma, J.; Wu, D.; Chen, B.; Du, C.; Liang, L.; Huang, Y.; Li, Z.; Rao, F.; Chen, G.; Liu, Z. Constructing Flexible Film Electrode with Porous Layered Structure by MXene/SWCNTs/PANI Ternary Composite for Efficient Low-Grade Thermal Energy Harvest. *Adv. Funct. Mater.* **2023**, *33*, No. 2209806.
(55) Ding, Z.; Du, C.; Long, W.; Cao, C.-F.; Liang, L.; Tang, L.-C.; Chen, G. Thermoelectrics and thermocells for fire warning applications. *Sci. Bull.* **2023**, *68*, 3261−3277.
(56) Lu, X.; Mo, Z.; Liu, Z.; Hu, Y.; Du, C.; Liang, L.; Liu, Z.; Chen, G. Robust, Efficient, and Recoverable Thermocells with Zwitterion-Boosted Hydrogel Electrolytes for Energy-Autonomous and Wearable Sensing. *Angew. Chem., Int. Ed.* **2024**, *63*, No. e202405357.

https://doi.org/10.1021/acssuschemeng.4c10855
ACS Sustainable Chem. Eng. 2025, 13, 4231−4241

(57) Qian, X.; Ma, Z.; Huang, Q.; Jiang, H.; Yang, R. Thermodynamics of Ionic Thermoelectrics for Low-Grade Heat Harvesting. *ACS Energy Lett.* **2024**, *9*, 679−706.
(58) Peng, P.; Zhou, J.; Liang, L.; Huang, X.; Lv, H.; Liu, Z.; Chen, G. Regulating thermogalvanic effect and mechanical robustness via redox ions for flexible quasi-solid-state thermocells. *Nano-Micro Lett.* **2022**, *14*, No. 81.
(59) Buckingham, M. A.; Zhang, S.; Liu, Y.; Chen, J.; Marken, F.; Aldous, L. Thermogalvanic and thermocapacitive behavior of superabsorbent hydrogels for combined low-temperature thermal energy conversion and harvesting. *ACS Appl. Energy Mater.* **2021**, *4*, 11204−11214.
(60) Hsu, C. C.; Lin, Y. T.; Hong, S. H.; Jeng, U. S.; Chen, H. L.; Yu, J.; Liu, C. L. 3D Printed Gelatin Methacrylate Hydrogel-Based Wearable Thermoelectric Generators. *Adv. Sustainable Syst.* **2024**, *8*, No. 2400039.
(61) Hong, S.-H.; Hsu, C.-C.; Liu, T.-H.; Lee, T.-C.; Tung, S.-H.; Chen, H.-L.; Yu, J.; Liu, C.-L. Extremely large Seebeck coefficient of gelatin methacryloyl (GelMA)-based thermogalvanic cells by the dual effect of ion-induced crystallization and nanochannel control. *Mater. Today Energy* **2024**, *42*, No. 101546.
(62) Lu, X.; Xie, D.; Zhu, K.; Wei, S.; Mo, Z.; Du, C.; Liang, L.; Chen, G.; Liu, Z. Swift assembly of adaptive thermocell arrays for device-level healable and energy-autonomous motion sensors. *Nano-Micro Lett.* **2023**, *15*, No. 196.
(63) Huggins, R. A. Simple method to determine electronic and ionic components of the conductivity in mixed conductors a review. *Ionics* **2002**, *8*, 300−313.
(64) Wang, S.; Yan, M.; Li, Y.; Vinado, C.; Yang, J. Separating electronic and ionic conductivity in mix-conducting layered lithium transition-metal oxides. *J. Power Sources* **2018**, *393*, 75−82.
(65) Sha, W.; Wang, Y.; Xiao, M.; Fang, Y.; Zhu, P.; Wang, Z.; Wang, S.; Zeng, W.; Zhao, J.; Ruan, L. Conductive ionic thermoelectric hydrogel with negative Seebeck coefficient, self-healing and highly sensitive to temperature for photothermoelectric conversion and non-contact sensing device. *Chem. Eng. J.* **2024**, *501*, No. 157823.

https://doi.org/10.1021/acssuschemeng.4c10855
ACS Sustainable Chem. Eng. 2025, 13, 4231−4241